

# Templating Effect for Organic Heterostructure Film Growth: Perfluoropentacene on Diindenoperylene

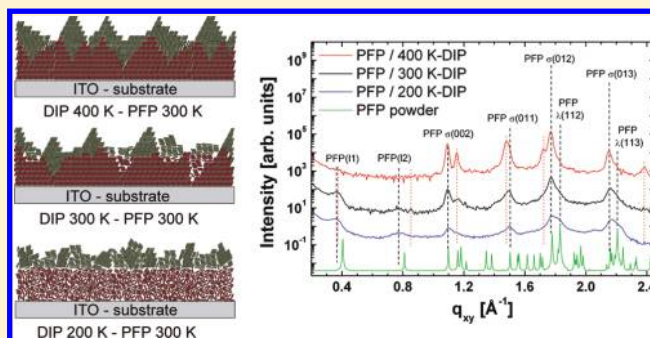
Alexander Hinderhofer,<sup>\*,†</sup> Takuya Hosokai,<sup>†,§</sup> Christian Frank,<sup>†</sup> Jiří Novák,<sup>‡</sup> Alexander Gerlach,<sup>†</sup> and Frank Schreiber<sup>\*,†</sup>

<sup>†</sup>Institut für Angewandte Physik Universität Tübingen, Auf der Morgenstelle 10, 72076 Tübingen, Germany

<sup>‡</sup>ESRF, BP 220, F-38043 Grenoble, France

<sup>§</sup>Department of Materials and Science, Iwate University, Ueda 4-3-5, Morioka 020-8551, Japan

**ABSTRACT:** We present a systematic study of templating effects in organic heterostructure growth, that is, where the growth behavior of the top layer is significantly influenced by the structural and morphological properties of the bottom layer. We prepared thin films of the donor material diindenoperylene (DIP) differing in crystal structure, grain size, and grain orientation on indium tin oxide (ITO). The acceptor material perfluoropentacene (PFP) was chosen to be evaporated on DIP to form the heterostructure. We employed X-ray reflectivity and grazing incidence X-ray diffraction as well as atomic force microscopy to investigate the heterostructures. The structure and morphology of the PFP layers depend on the properties of the DIP layer underneath. Two main effects were observed: PFP molecules in the top layer tend to adopt the orientation of the DIP molecules in the bottom layer and the crystalline quality of the PFP layer correlates with the crystalline quality of the DIP layer underneath in terms of the in-plane coherent crystal size.



## INTRODUCTION

Organic heterostructure devices, such as organic photovoltaic cells or organic light-emitting diodes, have shown promising results, but their growth behavior is not completely understood yet. Important for device performance of organic heterostructures are, inter alia, the crystal structure and morphology at the organic–organic heterointerface, since the contact area has a strong impact on charge carrier generation and transport.<sup>1–3</sup>

It is well-known that the growth of single organic films is already nontrivial due to orientational degrees of freedom of organic molecules and a subtle interplay between the intermolecular and substrate-molecule interaction.<sup>4–9a,9b</sup> The growth of organic heterostructures is still more complex. Depending on the organic bottom layer (here called templating layer), overlayer molecules can exhibit a change in molecular orientation<sup>10–15</sup> or different film morphology (e.g., domain size or roughness).<sup>16–23</sup> However, one important question, which still remains elusive, is the influence of roughness, domain size and crystallinity of the templating layer for the growth of its top layer in organic heterostructure.<sup>14,23</sup> In the present paper, the effect of templating was studied on a series of heterostructures where the properties of the bottom layer were systematically varied via growth temperature, while the growth conditions of the top layer were identical.

For the bottom layers, the organic donor material diindenoperylene<sup>9,24–28</sup> (DIP, Figure 1) is used. DIP was shown to have excellent performance as a hole conductor for photovoltaic applications.<sup>29</sup> For the top layer, we chose the organic

acceptor material perfluoropentacene (PFP, Figure 1), which is a promising candidate for organic solar cells due to its high ionization potential<sup>30</sup> and high electron mobility and has recently been the subject of intense work.<sup>31–36</sup> The combination of PFP and DIP in a heterostructure allows light absorption in a broad range of the visible spectrum<sup>24,37</sup> and may therefore be considered as a promising combination for organic photovoltaics. As a substrate, we chose indium tin oxide (ITO) coated glass slides, since this kind of substrate is widely used as transparent electrode for electronic devices including organic photovoltaic cells. In the present paper, we focus on the structure formation of the PFP/DIP/ITO system.

## EXPERIMENTAL SECTION

The samples were analyzed with in situ X-ray reflectivity (XRR) and grazing incidence X-ray diffraction (GIXD), which probe the structure of thin films perpendicular and parallel to the substrate plane, respectively. All X-ray measurements were performed with synchrotron light ( $\lambda = 0.092$  nm) at the ID10B beamline at the ESRF in Grenoble (France). For GIXD, the angle of incidence and the detector angle in the out-of-plane direction were kept at  $0.1^\circ$  corresponding to  $q_z = 0.0238 \text{ \AA}^{-1}$ . Data in the  $q_{xy}$  direction were collected by scanning the in-plane detector angle using a point detector. Thin films of DIP ( $C_{32}H_{16}$ ) and PFP

**Received:** March 31, 2011

**Revised:** May 18, 2011

**Published:** June 07, 2011

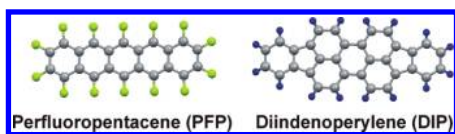


**Figure 1.** Chemical structure of perfluoropentacene ( $C_{22}F_{14}$ ) and diindenoperylene ( $C_{32}H_{16}$ ).

( $C_{22}F_{14}$ ) (Figure 1) were grown on ITO-coated glass substrates (ITO thickness: 130 nm, surface roughness  $\sigma_{rms} = 1$  nm) by thermal evaporation under UHV conditions, using a home-built portable vacuum chamber with beryllium-window.<sup>38</sup> Before deposition, the ITO substrates were cleaned ultrasonically with acetone, isopropanol, and ultrapure water, followed by heating to 700 K in the UHV growth chamber. The growth rate of both molecular thin films were set to 0.1–0.2 nm/min monitored by a water-cooled quartz crystal microbalance calibrated by X-ray reflectivity. To obtain different film structures of DIP the substrate temperature was varied between  $T = 200$ –400 K during growth by a combination of liquid nitrogen cooling and resistive heating of the sample holder. The X-ray measurements and PFP growth on DIP films were conducted in situ at 300 K for all films. Modeling and fitting of X-ray reflectivity data were performed with the MOTOFIT<sup>39</sup> software applying the Parratt formalism. Lower limits of the in-plane coherent crystal sizes  $l_s$  were determined by the Scherrer formula  $l_s = (fwhm)^{-1}(0.9394K_s)$ , where  $K_s = 1.0747$  is the Scherrer constant for spherical grains and fwhm is the full width half-maximum of the peak in  $\text{\AA}^{-1}$  determined with a Gaussian fit-function.<sup>40</sup> The instrumental broadening of the diffractometer was not included in the calculation, therefore only lower limits of  $l_s$  are given.

Atomic force microscopy (AFM) was performed within one week after film preparation with a JPK Nanowizard II using the noncontact dynamic mode with the amplitude as feedback lock-in parameter.

## RESULTS AND DISCUSSION

**Temperature Dependence of DIP Film Growth.** Here, we discuss the structure of the different DIP films, since this information is vital for the evaluation of templating effects described in the next section. Figure 2a shows the GIXD data of the DIP films (thickness:  $\sim 20$  nm) grown at  $T = 200$ , 300, and 400 K, which are compared with powder spectra of the DIP high temperature phase (HT-phase, P21/a polymorph) and the DIP low-temperature phase (LT-phase, P-1 polymorph, 298 K),<sup>41</sup> respectively. First, we discuss the assignment of the observed features in Figure 2a. According to ref 41, the features marked with  $\sigma$  or  $\lambda$  are assigned to the HT-phase. The  $\sigma$  features are attributed to domains with the  $ab$ -unit cell plane parallel to the substrate surface (standing molecules), and the  $\lambda$  features are domains with the  $ab$ -unit cell plane not parallel to the substrate surface (index  $l \neq 0$ , lying or tilted orientation). The inset of Figure 2b illustrates the orientation of the  $\sigma$ - and  $\lambda$ -domains. The broad  $\lambda(001)$  reflection in the 200 K film is probably superposed with the (001)-reflection from the LT-phase at  $q_{xy} = 0.43 \text{ \AA}^{-1}$  (marked by LT). Two small features denoted by  $LT^*$ , might stem either from the DIP LT-phase, or possibly a yet unknown DIP polymorph.

The domain composition of the DIP films extracted from the relative GIXD peak intensities depends strongly on  $T$ . For  $T = 400$  K, the DIP films consist almost exclusively of  $\sigma$ -domains. For  $T = 300$  K the  $\sigma$  features are weaker and broader, however, the  $\lambda$

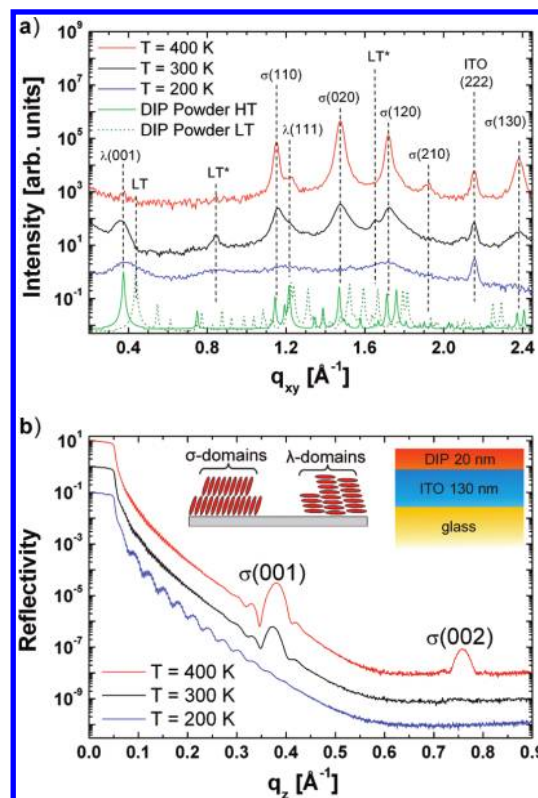


**Figure 2.** (a) GIXD and (b) XRR data of DIP films grown on ITO at different substrate temperatures. For clarity data sets are vertically shifted. The thickness of all films is  $\sim 20$  nm. The powder data of the DIP HT- and LT-phase at the bottom of panel a were calculated from the crystal structures reported in ref 41. The insets in panel b illustrate the layer stacking and the orientation of the  $\sigma$ - and  $\lambda$ -domains.

**Table 1.** Roughness  $\sigma_{rms}$  and Lower Limits of the in-Plane Coherent Crystal Sizes  $l_s$  of DIP  $\lambda$ - and  $\sigma$ -Domains for 20 nm Films Grown at Different  $T^a$

	400 K-DIP	300 K-DIP	200 K-DIP
$l_s$ DIP $\sigma$ -domains [nm]	27	13	3.0
$l_s$ DIP $\lambda$ -domains [nm]	27	8.0	5.0
$l_s$ PFP $\sigma$ -domains [nm]	34	28	18
$\sigma_{rms}$ [nm] of DIP	3.2 ( $\pm 0.4$ )	2.6 ( $\pm 0.3$ )	0.45 ( $\pm 0.1$ )
$\sigma_{rms}$ [nm] of PFP	4.6 ( $\pm 0.4$ )	3.9 ( $\pm 0.4$ )	3.7 ( $\pm 0.4$ )

<sup>a</sup> In addition  $\sigma_{rms}$  and  $l_s$  of  $\sigma$ -domains of 20 nm PFP films grown on three different DIP films are summarized.

features become more intense (e.g.,  $\lambda(001)$ ), which indicates preferred nucleation of the  $\lambda$ -domains at  $T = 300$  K. Detecting only the two  $\lambda$ -reflections with the highest structure factors of the HT-phase ((001) and (111)), we assume that  $\lambda$ -domains with other orientations are also existing, but the scattered intensity is below the background. For  $T = 200$  K, the film consists of  $\lambda$ -domains with a high degree of disorder derived from the peak widths, while the growth of the  $\sigma$ -domains is completely suppressed.

From the peak width of the in-plane Bragg reflections, the in-plane coherent crystal size  $l_s$  of the  $\sigma$ - and  $\lambda$ -domains of the three films is estimated (Table 1). For  $T = 400$  K  $l_s$  of the  $\lambda$ - and  $\sigma$ -domains is similar but decreases significantly when lowering  $T$ . This result indicates that  $T$  is critical for the growth of both the

$\lambda$ - and  $\sigma$ -domains on ITO. Similar growth behaviors of DIP were also found for other substrates.<sup>9,42–45</sup>

Figure 2b shows complementary XRR data from the DIP films discussed above. The XRR again shows a clear  $T$  dependence. For growth at  $T = 400$  K, two Bragg reflections are observed at  $q_z = 0.38 \text{ \AA}^{-1}$  and  $q_z = 0.76 \text{ \AA}^{-1}$  assigned to the  $\sigma(001)$  and  $\sigma(002)$  reflections. Compared to these, the intensity of the  $\sigma(001)$  reflection is significantly smaller in the 300 K-DIP film. Furthermore, for the 200 K-DIP film no Bragg reflection in the  $q_z$  direction is observed. These observations confirm the  $T$  dependence in  $\sigma$ -domain nucleation for the DIP films, in good agreement with the results from GIXD (Figure 2a).

Rocking scans on the  $\sigma(001)$  reflections were used to determine the mosaicity of the  $\sigma$ -domains (not shown). The mosaicity was found to be essentially equal ( $0.03 \pm 0.01^\circ$ ) for the 300 and 400 K-DIP films. From this result, we conclude that the decreasing intensity of the  $\sigma(00L)$  reflections at lower  $T$  is attributed to a smaller coherent scattering volume of the  $\sigma$ -domains in these films, that is, the crystallinity is reduced due to disorder and/or differently oriented crystallites replace the  $\sigma$ -domains with lowering of  $T$ .

The low crystallinity of films grown at low  $T$  results in a relatively low root-mean-squared roughness  $\sigma_{\text{rms}}$  of the surface as summarized in Table 1.  $\sigma_{\text{rms}}$  is determined from AFM data shown in Figure 4a–f. Where possible, we double-checked the obtained  $\sigma_{\text{rms}}$  values due to fitting the reflectivity curves (Figure 2b) in the region  $q_z = 0.07$  to  $0.2 \text{ \AA}^{-1}$  where the thickness interference oscillations occur. Details of the fitting procedure are described in the Appendix.

For DIP growth, we found that lowering  $T$  induces disorder and a smooth surface. Such a behavior at low temperatures is commonly observed for organic thin film growth due to reduction of surface diffusion of the adsorbates.<sup>46</sup> In the next section, we elucidate how the different film structures of the DIP templating layers affect the PFP film growth.

**Characterization of DIP/PFP Heterostructures.** Figure 3a shows GIXD data of PFP/DIP heterostructures. The PFP films (thickness:  $\sim 20$  nm) were grown at 300 K on each DIP film to study the templating effect of the DIP layers. All three heterostructures exhibit several in-plane Bragg reflections corresponding to the PFP thin film phase, marked with  $\sigma$  and  $\lambda$  in Figure 3a.<sup>47,48</sup>

All PFP  $\sigma$ -reflections stem from nearly standing PFP-molecules, which corresponds to an alignment of the  $bc$ -plane of the unit cell parallel to the substrate plane, while the PFP  $\lambda$ -reflections stem from crystallites that adopt a tilted or lying orientation. The observed PFP  $\lambda$ -reflections ( $\lambda(112)$ ,  $\lambda(113)$ ) have the largest structure factor of all PFP Bragg reflections (Figure 3a). In analogy to the DIP growth described above, we assume that PFP  $\lambda$ -domains with other orientations may also be present. These reflections are not observed, because due to the lower structure factor their intensity is below the background in our data.

Two additional Bragg reflections at  $q_{xy} = 0.37 \text{ \AA}^{-1}$  and  $q_{xy} = 0.77 \text{ \AA}^{-1}$  are tentatively assigned as PFP(11) and PFP(12), and correspond to an in-plane lattice spacing of 1.7 nm. This spacing is roughly consistent with the length of a PFP-molecule but not with that of the PFP thin film phase (1.58 nm). Therefore we speculate that the PFP(11,12) reflections stem from domains with molecules in lying orientation. We note that the PFP(11) reflection is superimposed with the DIP  $\lambda(001)$  reflection. Due to the small penetration depth of the evanescent wave in GIXD

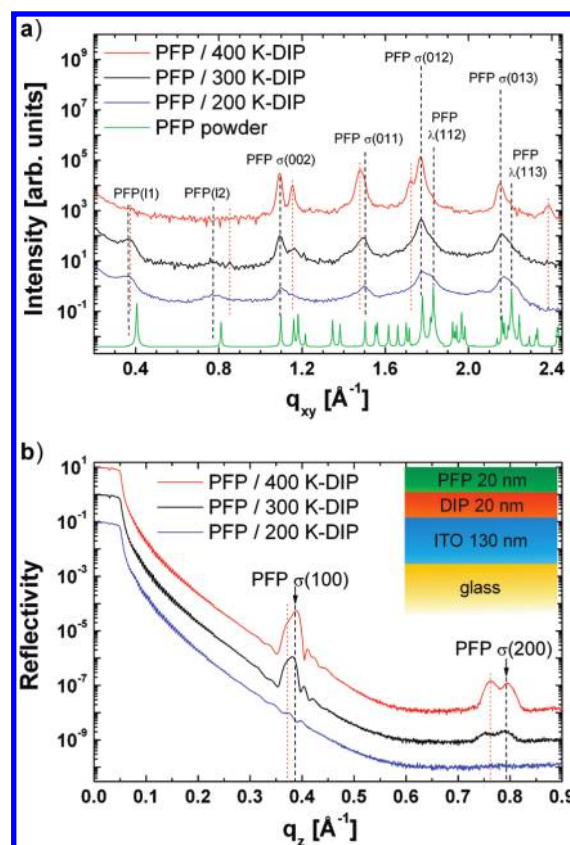


**Figure 3.** (a) GIXD and (b) XRR data of PFP films grown on different DIP films as discussed in the former section. For clarity data sets are vertically shifted. The thickness of each PFP layer is 20 nm. The red dotted lines indicate reflections from the DIP bottom layer (see Figure 2). The PFP powder data at the bottom of panel a were calculated from the crystal structure reported in ref 31.

experiments, only 20% of the intensity of the reflection marked as PFP(11) are contributed by the DIP  $\lambda(001)$  reflection.

The domain composition of the PFP films depends strongly on the DIP films. On the 400 K-DIP film, PFP  $\sigma$ -domains are dominantly observed. On the low  $T$  DIP films, PFP  $\sigma$ -domains are increasingly replaced by  $\lambda$ -domains and lying PFP(11,12), as illustrated at the bottom in Figure 4.

Since DIP and PFP in-plane reflections from lying PFP(11,12) and PFP  $\lambda$ -domains are mostly superimposed, we determined  $l_s$  only for the PFP  $\sigma$ -domains (Table 1). For PFP,  $l_s$  differs by a factor of  $\sim 2$  for the 400 K-DIP and the 200 K-DIP templating layer. Since the growth parameters for PFP evaporation are identical, the difference in  $l_s$  is induced by the different surface conditions of the DIP films underneath.

For two heterostructures (400 and 300 K-DIP), the XRR data (Figure 3b) exhibit two superimposed first order Bragg reflections around  $q_z \approx 0.38 \text{ \AA}^{-1}$ , which originate from DIP ( $\sigma(001)$ , HT-phase;  $d_{\perp} = 1.66$  nm) and from PFP ( $\sigma(100)$  thin film phase,  $d_{\perp} = 1.57$  nm).<sup>47</sup> These lattice spacings were determined from the second order Bragg reflections around  $q_z \approx 0.78 \text{ \AA}^{-1}$ , because there both reflections are easier to separate. The PFP layer grown on the 200 K-DIP film shows no clear Bragg reflection in the out-of-plane direction, similar to the 200 K-DIP film underneath (Figure 2b). The intensity of the PFP Bragg reflections is smaller for PFP growth on the low  $T$  DIP layers. This is again easy to observe at the second order Bragg

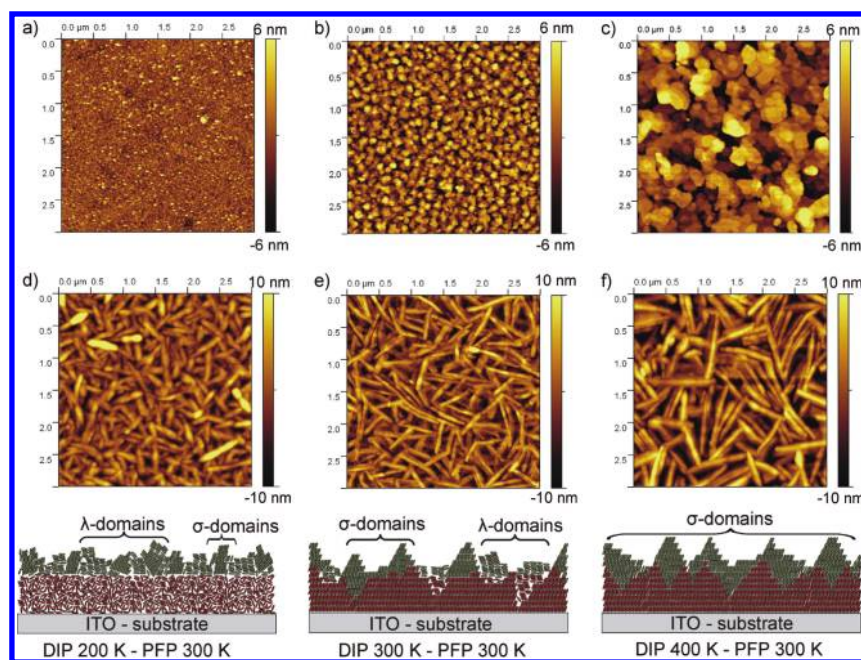


**Figure 4.** AFM images of differently prepared DIP films and heterostructures: (a) DIP grown at  $T = 200$  K. (b) DIP grown at  $T = 300$  K. (c) DIP grown at  $T = 400$  K. (d) PFP film grown on 200 K-DIP. (e) PFP film grown on 300 K-DIP. (f) PFP film grown on 400 K-DIP. At the bottom, sketches of the three PFP-DIP heterostructures are shown.

reflections. These observations are consistent with the GIXD data and demonstrate that the growth of PFP  $\sigma$ -domains is suppressed for the low  $T$  DIP templates.

Figure 4a–f show AFM images of the DIP bottom layers (a–c) and the three heterostructures (d–f). The DIP templates exhibit nearly circular grains for all temperatures. The grain size  $d$  varies strongly with  $T$  from  $d_s \sim 350$  nm at 400 K to  $d_s \sim 30$  nm at 200 K. The heterostructures exhibit needle-shaped PFP grains, which were observed also for PFP growth on other substrates.<sup>37,49</sup> However, it is seen that the domain size is reduced significantly for the low  $T$  DIP layers. The needle width is  $d_w \sim 120$  nm for all PFP layers, while the average length of the needle-like domains  $d_l$  varies significantly between  $d_l \sim 200$  nm for PFP on the 200 K-DIP layer and  $d_l \sim 1000$  nm for PFP on the 400 K-DIP layer.

Here, we would like to stress the difference of the morphological grain size  $d_s$  extracted from AFM images and the in-plane coherent crystal size  $l_s$ , which is the lower limit of the coherently ordered crystal size obtained from GIXD data. For organic thin films,  $l_s$  is frequently smaller than  $d_s$ , since single large grains visible in AFM images consist of several subdomains divided by dislocations.<sup>50–53</sup>

From the AFM images we determined the roughness  $\sigma_{\text{rms}}$  of all heterostructures. The results are summarized in Table 1. Compared to the DIP layers (Table 1), the  $\sigma_{\text{rms}}$  values of the heterostructures are significantly increased owing to the pronounced needle formation. Remarkably, the roughness increase is strongest for PFP/200 K-DIP heterostructure, although the 200 K-DIP film has the smoothest surface of all DIP films. This effect can be attributed to pronounced 3d growth of the  $\lambda$ -domains, where  $\sigma$ -domains seem to grow with slower roughening.<sup>49</sup>

In the following, we summarize the observed changes in growth of PFP induced by templating. For an overview, a sketch of the complete heterostructures is depicted at the bottom of Figure 4.

First, orientational templating is found. PFP evaporated on the 400 K-DIP film, which consists nearly completely of DIP  $\sigma$ -domains, nucleates nearly exclusively as  $\sigma$ -domains. In contrast, the PFP films grown on 300 K-DIP and 200 K-DIP exhibit less standing molecules. With the appearance of DIP crystallites with other orientations in the templating layer ( $\lambda$ -domains),  $\lambda$ -domains in the PFP layer correspondingly increase. In addition, PFP-domains oriented with the long molecular axis parallel to the substrate are found (11,12-reflections). These lying PFP crystallites appear only for the 200 K-DIP and 300 K-DIP templating layers, which exhibit a significant amount of disorder and DIP in  $\lambda$ -orientation. We speculate that the strong arene–perfluoroarene interaction is responsible for the orientational templating, which generally favors displaced  $\pi$ – $\pi$  stacking of arenes and perfluoroarenes.<sup>54,55</sup> In thermal equilibrium, PFP molecules on top of lying DIP molecules therefore would be expected to also lie down to form the energetically most favorable configuration. Thus, a lying PFP “seed”-layer is formed which leads to further nucleation of PFP in a lying orientation. If the templating layer consists of mostly standing DIP, impinging PFP molecules have a large diffusion length on the locally flat DIP terraces and nucleate preferably between the DIP ridges.<sup>17</sup> There, the PFP molecules nucleate most likely with a standing orientation at step edges exposing standing DIP molecules. Therefore, we conclude that growth of oriented PFP fibers is enhanced by an highly orientated DIP layer and is disturbed by differently oriented DIP crystallites.

Second, we observe a correlation between the crystalline quality of the DIP bottom layer and the PFP top layer. The in-plane coherent island size  $l_s$  of the PFP  $\sigma$ -domains varies with that of the DIP  $\sigma$ -domains. Because of this effect, the PFP in-plane coherent island size can be changed by a factor of  $\sim 2$ . Observing this effect and the orientational templating described above, we conclude that the interaction between PFP and DIP molecules at the interface is relatively strong. However, since the

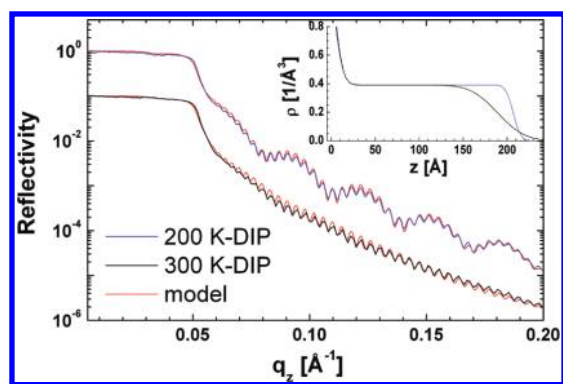


**Figure 5.** Reflectivity fits for extracting thickness and  $\sigma_{\text{rms}}$  of DIP films grown on ITO at 200 and 300 K. The inset shows electron density ( $\rho$ ) profiles of both models.

PFM domains (both  $l_s$  obtained from GIXD and  $d_s$  obtained from AFM) are significantly larger than the DIP domains of the bottom layer (Table 1), the growing PFM domains can to some extent overcome the domain boundaries of DIP at later growth stages. We speculate that this effect increases toward larger PFM thicknesses and leads to a structural decoupling of both layers. For growth of  $\text{F}_{16}\text{CoPc}$  on DIP, it was shown that this structural decoupling of the first and second material is faster when the terraces of the bottom material are larger than the intrinsic diffusion length of the second material.<sup>22</sup> However, for PFM growth on DIP, which is presented here, the diffusion length of PFM seems to be higher than the terrace sizes of DIP. Therefore, we find here a pronounced dependence of the crystal quality of the top layer from the crystal quality of the bottom layer.

Third, we tested whether the surface roughness of the different DIP layers has an impact on the crystalline quality of the PFM. The surface of the disordered 200 K-DIP layer is significantly smoother than the 300 and 400 K-DIP layer (Table 1). The crystallinity and orientation of PFM grown on such a surface, however, is worse than for growth on rougher DIP films with better crystallinity. This means that the averaged  $\sigma_{\text{rms}}$  roughness is probably not a suitable parameter for predicting the growth behavior of the top layer. Instead, the sublayer or substrate island size appears to play a more important role for achieving highly crystalline oriented films, probably because large crystalline islands, as seen in Figure 4c, provide locally smooth nucleation sites. We note that the above findings are probably not independent. The fundamental effect may be orientational templating induced by strong attraction of the PFM and DIP molecules via interaction of the conjugated  $\pi$ -systems. This fundamental effect then leads to secondary effects like correlation between island sizes and modified roughening.

These findings have potentially a significant impact on device applications: The higher density of grain boundaries and vacancy sites in the PFM film grown on DIP layers with low crystallinity has a negative effect on the charge carrier mobility and the exciton diffusion length of these films.<sup>52,53</sup> In addition, the orientational change of crystal grains is important, since both the light absorption coefficient<sup>37</sup> and the energy level-alignment<sup>56</sup> are strongly related to the molecular orientation.

## SUMMARY

In summary, the crystalline quality and molecular orientation of DIP films grown on ITO can be tuned by the substrate

temperature during growth. PFM grown on differently prepared DIP layers exhibit two kinds of templating. First, orientational templating, that is, the PFM molecules, adopt at least partly the orientation of DIP molecules. Second, both the domain size as well as the crystalline quality of PFM scales with the domain size and crystalline quality of the DIP films underneath.

## APPENDIX - ROUGHNESS DETERMINATION OF DIP FILMS

Here the determination of  $\sigma_{\text{rms}}$  for the organic thin films is described. The roughness were determined for all films from AFM data. In addition,  $\sigma_{\text{rms}}$  of the 200 K-DIP and 300 K-DIP were determined independently via fitting the X-ray reflectivity curve near the total reflection edge. We found that the  $\sigma_{\text{rms}}$  values from both techniques are consistent.<sup>28</sup> Figure 5 shows reflectivity fits for extracting thickness and roughness ( $\sigma_{\text{rms}}$ ) of DIP films grown on ITO. Electron density ( $\rho$ ) profiles are shown in the inset. The superimposed small oscillations in Figure 5 stem from the 130 nm ITO layer underneath the DIP.

## AUTHOR INFORMATION

### Corresponding Author

\*E-mail: (A.H.) alexander.hinderhofer@uni-tuebingen.de; (F.S.) frank.schreiber@uni-tuebingen.de.

## ACKNOWLEDGMENT

We acknowledge the DFG for support and the ESRF for provision of synchrotron radiation. T. Hosokai was supported by the Alexander von Humboldt foundation. We thank P. Fenter for fruitful discussions.

## REFERENCES

- (1) Peumans, P.; Yakimov, A.; Forrest, S. R. *J. Appl. Phys.* **2003**, *93*, 3693–3723.
- (2) Brütting, W.; Berleb, S.; Mückel, A. G. *Org. Electron.* **2001**, *2*, 1–36.
- (3) Yi, Y.; Coropceanu, V.; Brédas, J.-L. *J. Am. Chem. Soc.* **2009**, *131*, 15777–15783.
- (4) Schreiber, F. *Phys. Status Solidi* **2004**, *201*, 1037.
- (5) Witte, G.; Wöll, C. *J. Mat. Res.* **2004**, *19*, 1889–1916.
- (6) Ruiz, R.; Choudhary, D.; Nickel, B.; Chang, T. T. K.; Mayer, A.; Clancy, P.; Blakely, J. M.; Headrick, R. L.; Iannotta, S.; Malliaras, G. G. *Chem. Mater.* **2004**, *16*, 4497.
- (7) Krause, B.; Schreiber, F.; Dosch, H.; Pimpinelli, A.; Seeck, O. *Euro. Phys. Lett.* **2004**, *65*, 372.
- (8) Hlawacek, G.; Puschnig, P.; Frank, P.; Winkler, A.; Ambrosch-Draxl, C.; Teichert, C. *Science* **2008**, *321*, 108–111.
- (9) (a) Kowarik, S.; Gerlach, A.; Sellner, S.; Schreiber, F.; Cavalcanti, L.; Kononov, O. *Phys. Rev. Lett.* **2006**, *96*, 125504. (b) Hosokai, T.; Gerlach, A.; Hinderhofer, A.; Frank, C.; Ligorio, G.; Heinemeyer, U.; Vorobiev, A.; Schreiber, F. *Appl. Phys. Lett.* **2010**, *97*, 063301.
- (10) Heutz, S.; Cloots, R.; Jones, T. S. *Appl. Phys. Lett.* **2000**, *77*, 3938–3940.
- (11) Oehzelt, M.; Koller, G.; Ivanco, J.; Berkebile, S.; Haber, T.; Resel, R.; Netzer, F.; Ramsey, M. *Adv. Mater.* **2006**, *18*, 2466–2470.
- (12) de Oteyza, D. G.; Barrena, E.; Sellner, S.; Ossó, J. O.; Dosch, H. *Surf. Sci.* **2007**, *601*, 4117–4121.
- (13) Koller, G.; Berkebile, S.; Krenn, J. R.; Netzer, F. P.; Oehzelt, M.; Haber, T.; Resel, R.; Ramsey, M. G. *Nano Lett.* **2006**, *6*, 1207–1212.
- (14) Sakurai, T.; Naito, R.; Toyoshima, S.; Ohashi, T.; Akimoto, K. *Nanosci. Nanotechnol. Lett.* **2009**, *1*, 23–27.

- (15) Naito, R.; Toyoshima, S.; Ohashi, T.; Sakurai, T.; Akimoto, K. *Jpn. J. Appl. Phys.* **2008**, *47*, 1416–1418.
- (16) Fenter, P.; Schreiber, F.; Bulovic', V.; Forrest, S. R. *Chem. Phys. Lett.* **1997**, *277*, 521–526.
- (17) Hinderhofer, A.; Gerlach, A.; Kowarik, S.; Zontone, F.; Krug, J.; Schreiber, F. *Europhys. Lett.* **2010**, *91*, S6002.
- (18) Barrena, E.; de Oteyza, D. G.; Sellner, S.; Dosch, H.; Osso, J. O.; Struth, B. *Phys. Rev. Lett.* **2006**, *97*, 076102.
- (19) Häming, M.; Greif, M.; Sauer, C.; Schöll, A.; Reinert, F. *Phys. Rev. B* **2010**, *82*, 235432.
- (20) de Oteyza, D. G.; Barrena, E.; Zhang, Y.; Krauss, T. N.; Turak, A.; Vorobiev, A.; Dosch, H. *J. Phys. Chem. C* **2009**, *113*, 4234–4239.
- (21) Ye, R.; Baba, M.; Suzuki, K.; Mori, K. *Appl. Surf. Sci.* **2008**, *254*, 7885–7888.
- (22) Zhang, Y.; Barrena, E.; Zhang, X.; Turak, A.; Maye, F.; Dosch, H. *J. Phys. Chem. C* **2010**, *114*, 13752–13758.
- (23) Yang, J.; Yan, D. *Chem. Soc. Rev.* **2009**, *38*, 2634–2645.
- (24) Heinemeyer, U.; Scholz, R.; Gisslén, L.; Alonso, M. I.; Ossó, J. O.; Garriga, M.; Hinderhofer, A.; S. Kowarik, M. K.; Gerlach, A.; Schreiber, F. *Phys. Rev. B* **2008**, *78*, 085210.
- (25) Zhang, D.; Heinemeyer, U.; Stanciu, C.; Sackrow, M.; Braun, K.; Hennemann, L. E.; Wang, X.; Scholz, R.; Schreiber, F.; Meixner, A. *J. Phys. Rev. Lett.* **2010**, *104*, 056601.
- (26) Heinemeyer, U.; Broch, K.; Hinderhofer, A.; Kytka, M.; Scholz, R.; Gerlach, A.; Schreiber, F. *Phys. Rev. Lett.* **2010**, *104*, 257401.
- (27) Gisslén, L.; Scholz, R. *Phys. Rev. B* **2009**, *80*, 115309.
- (28) Dürr, A. C.; Schreiber, F.; Ritley, K. A.; Kruppa, V.; Krug, J.; Dosch, H.; Struth, B. *Phys. Rev. Lett.* **2003**, *90*, 016104.
- (29) Wagner, J.; Gruber, M.; Hinderhofer, A.; Wilke, A.; Bröker, B.; Frisch, J.; Amsalem, P.; Vollmer, A.; Opitz, A.; Koch, N.; Frank, S.; Brütting, W. *Adv. Funct. Mater.* **2010**, *20*, 4295.
- (30) Koch, N.; Vollmer, A.; Duhm, S.; Sakamoto, Y.; Suzuki, T. *Adv. Mater.* **2007**, *19*, 112–116.
- (31) Sakamoto, Y.; Suzuki, T.; Kobayashi, M.; Gao, Y.; Fukai, Y.; Inoue, Y.; Sato, F.; Tokito, S. *J. Am. Chem. Soc.* **2004**, *126*, 8138.
- (32) Yokoyama, T.; Park, C. B.; Nishimura, T.; Kita, K.; Toriumi, A. *Jpn. J. Appl. Phys.* **2008**, *47*, 3643–3646.
- (33) Delgado, M. C. R.; Pigg, K. R.; da Silva Filho, D. A.; Gruhn, N. E.; Sakamoto, Y.; Suzuki, T.; Osuna, R. M.; Casado, J.; Hernandez, V.; Navarrete, J. T. L.; Martinelli, N. G.; Cornil, J.; Sanchez-Carrera, R. S.; Coropceanu, V.; Bredas, J.-L. *J. Am. Chem. Soc.* **2009**, *131*, 1502–1512.
- (34) Broch, K.; Heinemeyer, U.; Hinderhofer, A.; Anger, F.; Scholz, R.; Gerlach, A.; Schreiber, F. *Phys. Rev. B* **2011**, *83*, 245307.
- (35) Duhm, S.; Hosoumi, S.; Salzmänn, I.; Gerlach, A.; Oehzelt, M.; Wedl, B.; Lee, T.-L.; Schreiber, F.; Koch, N.; Ueno, N.; Kera, S. *Phys. Rev. B* **2010**, *81*, 045418.
- (36) Koch, N.; Gerlach, A.; Duhm, S.; Glowatzki, H.; Heimel, G.; Vollmer, A.; Sakamoto, Y.; Suzuki, T.; Zegenhagen, J.; Rabe, J. P.; Schreiber, F. *J. Am. Chem. Soc.* **2008**, *130*, 7300.
- (37) Hinderhofer, A.; Heinemeyer, U.; Gerlach, A.; Kowarik, S.; Jacobs, R. M. J.; Sakamoto, Y.; Suzuki, T.; Schreiber, F. *J. Chem. Phys.* **2007**, *127*, 194705.
- (38) Ritley, K. A.; Krause, B.; Schreiber, F.; Dosch, H. *Rev. Sci. Instrum.* **2001**, *72*, 1453–1457.
- (39) Andrew, N. *J. Appl. Crystallogr.* **2006**, *39*, 273–276.
- (40) Birkholz, M. *Thin Film Analysis by X-Ray Scattering*; Wiley-VCH: Weinheim, 2006.
- (41) Heinrich, M. A.; Pflaum, J.; Tripathi, A. K.; Frey, W.; Steigerwald, M. L.; Siegrist, T. *J. Phys. Chem. C* **2007**, *111*, 18878.
- (42) Dürr, A. C.; Koch, N.; Kelsch, M.; Rühm, A.; Ghijsen, J.; Johnson, R. L.; Pireaux, J.-J.; Schwartz, J.; Schreiber, F.; Dosch, H.; Kahn, A. *Phys. Rev. B* **2003**, *68*, 115428.
- (43) Schuster, B.-E.; Casu, M. B.; Biswas, I.; Hinderhofer, A.; Gerlach, A.; Schreiber, F.; Chassé, T. *Phys. Chem. Chem. Phys.* **2009**, *11*, 9000–9004.
- (44) Kowarik, S.; Gerlach, A.; Sellner, S.; Cavalcanti, L.; Kononov, O.; Schreiber, F. *Appl. Phys. A* **2009**, *95*, 233–239.
- (45) Dürr, A. C.; Schreiber, F.; Münch, M.; Karl, N.; Krause, B.; Kruppa, V.; Dosch, H. *Appl. Phys. Lett.* **2002**, *81*, 2276.
- (46) Witte, G.; Hänel, K.; Söhnchen, S.; Wöll, C. *Appl. Phys. A* **2006**, *82*, 447–455.
- (47) Salzmänn, I.; Duhm, S.; Heimel, G.; Rabe, J. P.; Koch, N.; Oehzelt, M.; Sakamoto, Y.; Suzuki, T. *Langmuir* **2008**, *24*, 7294–7298.
- (48) For PFP films, a single crystal phase ( $V = 797 \text{ \AA}^3$  at 173 K) and a slightly distorted thin film phase ( $V = 816 \text{ \AA}^3$  at room temperature) were reported. We assume that both structures have similar structure factors, since the unit cells of both are nearly identical. Indeed, the difference in both structures may be a pure temperature effect, since high anisotropic thermal expansion coefficients are not unusual for similar organic crystals.
- (49) Kowarik, S.; Gerlach, A.; Hinderhofer, A.; Milita, S.; Borgatti, F.; Zontone, F.; Suzuki, T.; Biscarini, F.; Schreiber, F. *Phys. Status Solidi RRL* **2008**, *2*, 120–122.
- (50) Nickel, B.; Barabash, R.; Ruiz, R.; Koch, N.; Kahn, A.; Feldman, L. C.; Haglund, R. F.; Scoles, G. *Phys. Rev. B* **2004**, *70*, 125401.
- (51) Kowarik, S.; Broch, K.; Hinderhofer, A.; Schwartzberg, A.; Ossó, J. O.; Kilcoyne, D.; Schreiber, F.; Leone, S. R. *J. Chem. Phys.* **2010**, *114*, 13061.
- (52) Nakamura, M.; Ohguri, H.; Goto, N.; Tomii, H.; Xu, M.; Miyamoto, T.; Matsubara, R.; Ohashi, N.; Sakai, M.; Kudo, K. *Appl. Phys. A* **2009**, *95*, 73–80.
- (53) Matsubara, R.; Sakai, M.; Kudo, K.; Yoshimoto, N.; Hirose, I.; Nakamura, M. *Org. Electron.* **2011**, *12*, 195–201.
- (54) Meyer, E. A.; Castellano, R. K.; Diederich, F. *Angew. Chem., Int. Ed.* **2003**, *42*, 1210–1250.
- (55) Hinderhofer, A.; Frank, C.; Hosokai, T.; Resta, A.; Gerlach, A.; Schreiber, F. *J. Chem. Phys.* **2011**, *134*, 104702.
- (56) Salzmänn, I.; Duhm, S.; Heimel, G.; Oehzelt, M.; Kniprath, R.; Johnson, R. L.; Rabe, J. P.; Koch, N. *J. Am. Chem. Soc.* **2008**, *130*, 12870–12871.